Additive Manufacturing: Metallurgy, Cut Analysis & Porosity

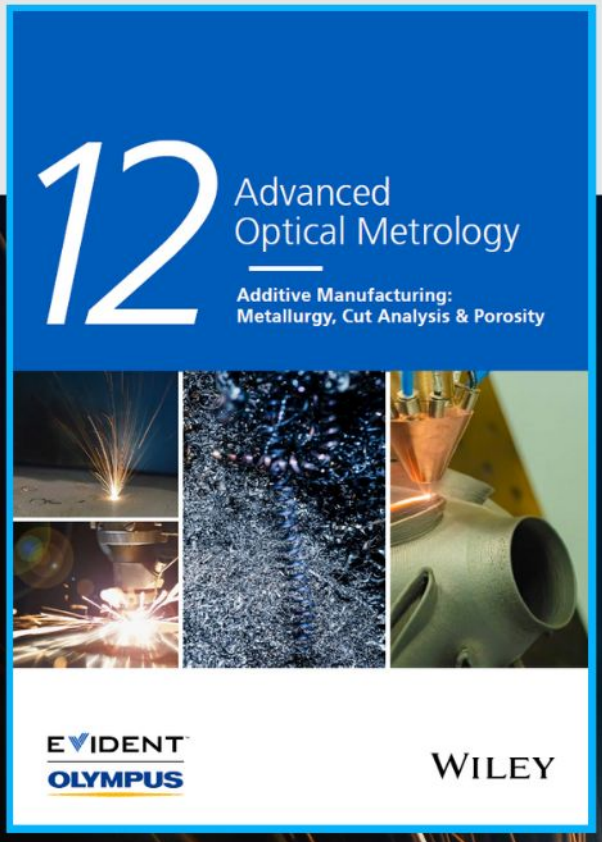

The latest eBook from Advanced Optical Metrology. Download for free.

In industry, sector after sector is moving away from conventional production methods to additive manufacturing, a technology that has been recommended for substantial research investment.

Download the latest eBook to read about the applications, trends, opportunities, and challenges around this process, and how it has been adapted to different industrial sectors.

EVIDENT
OLYMPUS

WILEY

NANO · MICRO small
www.small-journal.com

Enabling High-Stability of Aqueous-Processed Nickel-Rich Positive Electrodes in Lithium Metal Batteries

*Fanglin Wu, Matthias Kuenzel, Thomas Diemant, Angelo Mullaliu, Shan Fang, Jae-Kwang Kim, Hee Woong Kim, Guk-Tae Kim, and Stefano Passerini**

Lithium batteries occupy the large-scale electric mobility market raising concerns about the environmental impact of cell production, especially regarding the use of poly(vinylidene difluoride) (teratogenic) and *N*-methyl-2-pyrrolidone (NMP, harmful). To avoid their use, an aqueous electrode processing route is utilized in which a water-soluble hybrid acrylic-fluoropolymer together with sodium carboxymethyl cellulose is used as binder, and a thin phosphate coating layer is in situ formed on the surface of the nickel-rich cathode during electrode processing. The resulting electrodes achieve a comparable performance to that of NMP-based electrodes in conventional organic carbonate-based electrolyte (LP30). Subsequently, an ionic liquid electrolyte (ILE) is employed to replace the organic electrolyte, building stable electrode/electrolyte interphases on the surface of the nickel-rich positive electrode (cathode) and metallic lithium negative electrode (anode). In such ILE, the aqueously processed electrodes achieve high cycling stability with a capacity retention of 91% after 1000 cycles (20 °C). In addition, a high capacity of more than 2.5 mAh cm^{-2} is achieved for high loading electrodes (≈15 mg cm^{-2}) by using a modified ILE with 5% vinylene carbonate additive. A path to achieve environmentally friendly electrode manufacturing while maintaining their outstanding performance and structural integrity is demonstrated.

1. Introduction

In the course of the rapid expansion of lithium-ion batteries (LIBs) into electromobility and stationary energy storage applications, resolving outstanding concerns regarding health and the environment during the electrode fabrication process has become paramount.[1,2] The positive electrode processing of LIBs is mainly based on the use of toxic and suspected teratogenic *N*-methyl-2-pyrrolidone (NMP) as slurry solvent/dispersant and suspected mutagenic and teratogenic poly(vinylidene difluoride) (PVdF) as binder.[3] Under these circumstances, aqueous electrode processing has drawn much attention in recent years with the possibility to replace toxic chemicals by a sustainable water-soluble binder.[4] Specifically, styrene-butadiene rubber in combination with carboxymethyl cellulose (CMC) has been commercialized for graphite-based anode and exhibits a competitive or even superior electrochemical performance compared to the traditional PVdF-based electrode fabrication.[5,6] Nevertheless, further advancements are necessary to establish aqueous cathode processing on a large industrial scale. The main barrier is the reactivity of transition metal oxides with water to form hydroxides and consequently, the high pH basic slurry gives rise to severe corrosion of the aluminum current collector.[2] This phenomenon is accelerated with increasing nickel contents, accompanying lithium leaching from nickel-rich cathode materials,[7] which manifest a high surface reactivity.[8] The material spontaneously reacts with trace moisture and CO_2 to form LiOH and Li_2CO_3,[9] i.e., resulting in a slurry pH value typically greater than 12.[10] Therefore, this represents the immense difficulty to achieve high-energy density lithium batteries (high nickel content cathodes) as well as environmentally friendly aqueous electrode processing at the same time.

Recently, plenty of efforts have been made to employ water-soluble binders in high-energy cathodes. Sodium carboxymethyl cellulose (Na-CMC) was proven to be useful not only in anodes as a thickener, but also acting as the sole polymeric binder in cathodes, such as $LiNi_{1/3}Mn_{1/3}Co_{1/3}O_2$,[11] $LiNi_{0.4}Co_{0.2}Mn_{0.4}O_2$,[12] and interestingly, showed an improved cycling stability compared to PVdF-based electrodes attributed to the enhanced Li^+ diffusion kinetics and decreased polarization.[12] Furthermore, CMC was also used as binder in high-voltage (5 V) cathode materials like $LiNi_{0.4}Mn_{1.6}O_4$, which displayed a higher discharge capacity and lower self-discharge, however, accompanied

F. Wu, M. Kuenzel, T. Diemant, A. Mullaliu, S. Fang, G.-T. Kim, S. Passerini
Helmholtz Institute Ulm (HIU) Electrochemical Energy Storage
Helmholtzstrasse 11 89081, Ulm, Germany
E-mail: stefano.passerini@kit.edu

F. Wu, M. Kuenzel, T. Diemant, A. Mullaliu, S. Fang, G.-T. Kim, S. Passerini
Karlsruhe Institute of Technology (KIT)
P. O. Box 3640 76021, Karlsruhe, Germany

J.-K. Kim, H. W. Kim
Department of Solar & Energy Engineering
Cheongju University
Cheongju, Chungbuk 28503, Republic of Korea

The ORCID identification number(s) for the author(s) of this article can be found under https://doi.org/10.1002/smll.202203874.

DOI: 10.1002/smll.202203874

with worse cycling stability.[13] Then, Dong et al.[14] adapted another water-soluble binder, poly(methyl vinyl ether-alt-lithium maleic acid) in analogous 5 V-class $LiNi_{0.5}Mn_{1.5}O_4$ cathodes, which displayed superior adhesion and cohesion, and obtained a better cycle life and rate capability. This was attributed to the more favorable cathode electrolyte interphase layer formed on the particles covered with such binder and the improved contact with the current collector as also reported for similar binder systems.[15,16] However, regarding nickel-rich cathodes, there are only few reports making efforts on the aqueous electrode processing. Poly(acrylic acid)[17] may be a viable option because of its carboxyl groups (-COOH), which can neutralize the strong alkalinity inducing the pH value reverting back to ≈9, as well as simultaneously achieving an enhanced adhesion and improved slurry dispersion. Recently, an acrylic emulation was used as aqueous binder for $LiNi_{0.8}Co_{0.1}Mn_{0.1}O_2$ (NCM811) positive electrodes with excellent cycling stability, while still slightly lower capacities than for NMP-processed electrodes were obtained.[18]

Herein, we employed a hybrid polymer binder consisting of an acrylic and fluoropolymer (TRD202A) combined with Na-CMC (used as thickener to stabilize the slurry and adjust its viscosity) and assisted by a small amount of phosphoric acid (H_3PO_4) as slurry additive to protect the cathode particle surface as well as to avoid the corrosion of the aluminum current collector. On the other hand, the commercial electrolyte (LP30, 1 M $LiPF_6$ in ethylene carbonate (EC)/dimethyl carbonate (DMC), 1:1 by volume) would be susceptible to residual water as $LiPF_6$ reacts with trace moisture to form detrimental hydrogen fluoride, which will attack the cathode surface and accelerates material ageing and performance degradation.[19,20] Therefore, residual water is another issue for large-scale aqueous electrode processing, which requires either a high temperature for its complete removal[21] or lower dew points,[22] both increasing the production cost. These issues associated with the sensitivity of LP30 electrolyte toward trace moisture can be avoided using ionic liquid electrolytes (ILEs) with bis-sulfonylimide lithium salts.[20,23] In addition, the ionic liquid-based electrolyte was demonstrated to form a more stable cathode electrolyte interphase and solid electrolyte interphase on Li-metal anodes, therefore, a specifically tailored ILE ($0.8Pyr_{14}FSI$-0.2LiTFSI) is employed in water-processed electrodes. Additionally, the use of ILE tremendously improves the compatibility with lithium metal and battery safety, due to its nonvolatility and low-flammability.[24] Nevertheless, the ILE also faces challenges of low ionic conductivity and high viscosity, when applied to high mass loading electrodes; the wetting issue greatly hinders its battery performance, limiting its practicability toward commercialization. Therefore, the ILE was modified by introducing additives such as vinylene carbonate (VC) to reduce viscosity and enable higher room-temperature (RT) conductivities.

2. Results and Discussion

Currently, positive electrode manufacturing for LIBs is based on PVdF as binder and requires NMP as solvent (see **Figure 1**a). The application of this toxic solvent increases the cost for battery manufacturers since thorough ventilation and recovery systems are indispensable, as well as personal protection equipment. Nevertheless, a certain risk to environmental and personal health persists.[3] To overcome this challenge, herein, a hydrophilic acrylic- and fluoro-polymeric binder was employed to realize water-based electrodes. Furthermore, the whole electrode processing was conducted in an environmentally friendly aqueous route (Figure 1a). Despite growing expertise to prepare water-based electrodes of $LiFePO_4$[25] and low nickel content cathode materials,[11] it must be stressed that the high sensitivity of nickel-rich cathode materials to moisture makes the aqueous processing of such materials, without sacrificing their electrochemical performance, very challenging. Therefore, we adopted a facile one-pot in situ coating route to protect the nickel-rich cathode material (NCM811), which Rietveld refinement of the X-ray diffraction (XRD) pattern is shown in Figure S1 in the Supporting Information, and the refined atomic parameters are reported in Table S1 in the Supporting Information. For the coating, 1 wt% H_3PO_4 was added to the slurry during electrode processing (Figure 1b). Beyond its primary function to control the pH value and suppress the corrosion of the aluminum current collector, the phosphoric acid is also involved in acid–base reactions with surface residual lithium species (Li_2O, LiOH, Li_2CO_3).[26] In consequence, a Li_3PO_4 coating layer is generated on the surface of the cathode particles and protects them from degradation by water.[27] It is well-known that phosphates are good candidates for coatings of cathode materials[28,29] because of their high ionic conductivity and high chemical stability originating from the stable P=O bonds.[26] Therefore, phosphate-coated positive electrode materials are more resistant to water. We investigated the effect of aqueous processing on positive electrodes and compared two types of electrodes made via two different processing routes: An aqueous route with TRD 202A and CMC binder (named water-based electrode) and a nonaqueous route with PVdF binder using NMP solvent (named NMP-based electrode). First, the electrode interfaces were investigated by X-ray photoelectron spectroscopy (XPS), the results of the measurements in the C 1s, O 1s, and Ni 2p regions are compared in Figure 1c. In the C 1s spectrum of the water-based electrode, a small peak at ≈290.4 eV is observed, which is probably related to Li_2CO_3, and a neat peak at 288.7 eV associated with O−C=O species from the binder's carboxyl group. In comparison, the peak related to Li_2CO_3 is not detected in the spectrum of the NMP-based electrode (see Figure S2, Supporting Information); instead, a peak at ≈291.1 eV is found, which is related to the CF_2 groups of the PVdF binder. These findings are also corroborated by the spectra in the O 1s region. A strong M−O peak (at 529.7 eV) is observed for the NMP-based electrode, which has much higher intensity than for the water-based electrode. The M−O peak is associated with the oxygen of NCM,[2] hence, the lower intensity of this peak for the water-based electrode indicates the presence of a coating layer on the surface reducing the intensity of the M−O species. Similarly, a strong reduction of signal intensity was also observed for the water-based electrode in the Ni 2p region. Apart from the difference in intensity, the general shape and peak structure is comparable for the two electrodes, indicating a similar chemical state of the nickel in NCM for both samples. In the O 1s spectra, a strong peak at 533.3 eV is observed for the water-based electrode, which is mainly attributed to P−O−P (and C−O) species. The P−O−P species

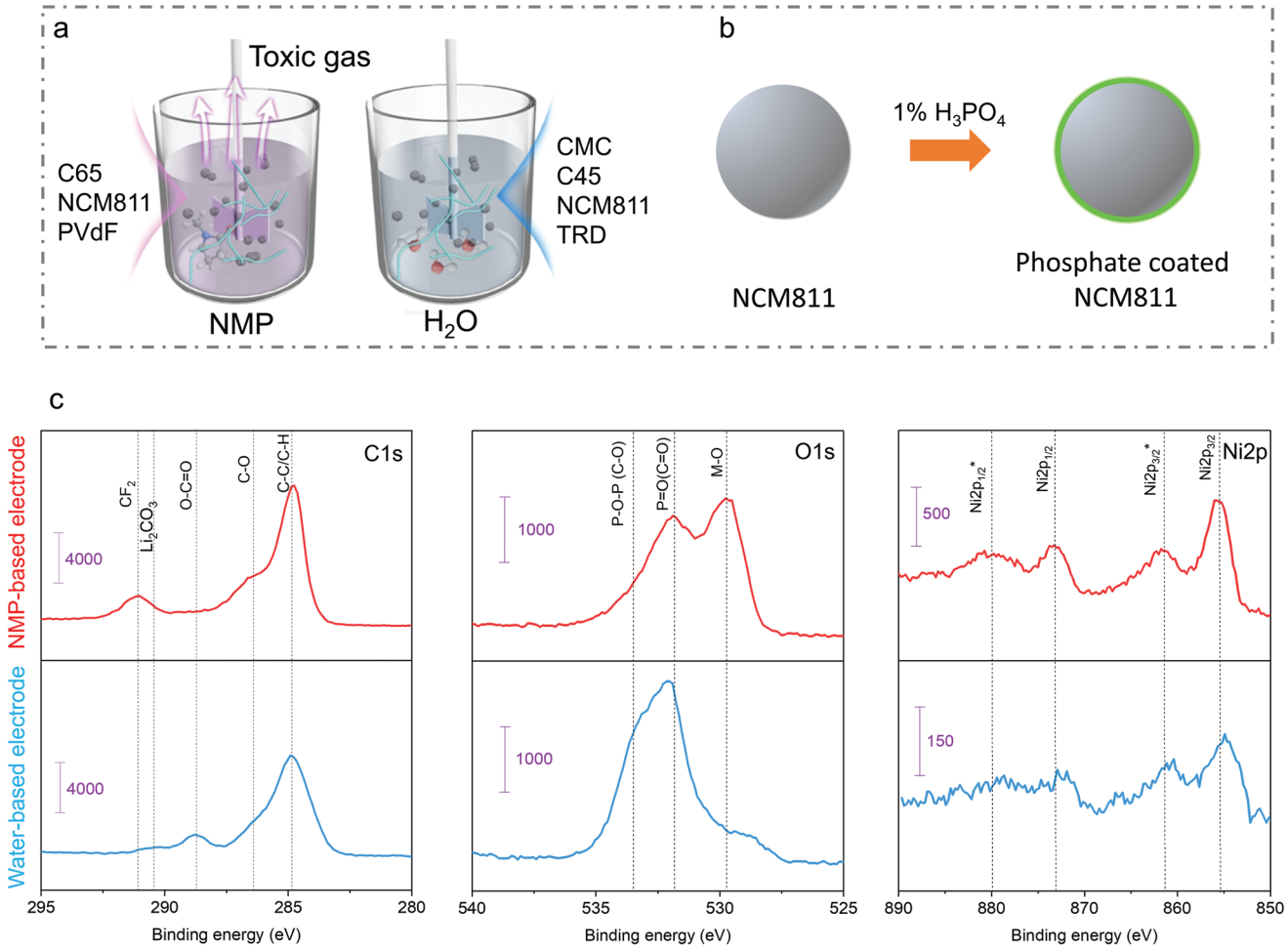

Figure 1. Comparison of the different routes for electrode processing employed in this study. Schematic illustration of a) traditional organic solvent-based (NMP-based) electrode processing and water-based electrode processing in this work. b) NCM811 particles in situ coated with a thin phosphate layer. c) XPS detail spectra in the C 1s, O 1s, and Ni 2p region of NMP-based (top) and water-based (bottom) electrodes using PVdF and TRD/CMC binder, respectively.

are associated with the phosphate compounds coated on the surface. In contrast, this feature is much less pronounced for the NMP-based electrode, which can be easily explained by the absence of a phosphate coating layer in this sample. Correspondingly, a peak due to phosphates is also observed in the P 2p spectrum of the water-based electrode at 133.3 eV (Figure S3, Supporting Information). Finally, the peak in the O 1s spectra at 531.8 eV is related to carbonates and hydroxides forming upon storage or preparation of the electrodes.[9] In addition, P=O species are also expected to contribute to this feature in the spectrum of the water-based electrode. Consequently, a slightly higher intensity of this peak is observed here. In other words, this suggests that no severe surface contamination has been induced during the aqueous electrode processing. To further investigate the composition and distribution of components on the cathode surfaces, scanning electron microscopy (SEM) with energy dispersive X-ray spectroscopy (EDX) measurements were performed (Figures S4–S6, Supporting Information). Figure S4 in the Supporting Information demonstrates a more homogenous distribution of conductive agent on the surface of the cathode particles in the water-based electrode using TRD/CMC as binder. While the conductive agent is mainly located around the secondary particles in the NMP-based electrode, the surface of particles appears very clean without a covering layer. In contrast, the surface of the particles in the water-based electrode is completely covered. It seems plausible that the uniform distribution of conductive agent is beneficial for lithium diffusion and electron conductivity. The mapping of carbon and fluorine elements further proves the distribution of conductive agent and binder (comparing Figures S5 and S6, Supporting Information). Furthermore, the mapping of phosphorus element confirms the uniform phosphate coating of the particles in the water-based electrode (Figure S6, Supporting Information). The detailed surface element compositions as derived by EDX analysis are compared in Table S2 in the Supporting Information. In summary, there is a thin coating layer consisting of Li_2CO_3 and phosphates together with conductive agent and binder formed on the surface of Ni-rich cathode particles in the water-based electrode.

Besides the effects of the two different processing routes on the electrode morphology and the active material surface, their impact on the electrochemical performance is the key challenge of this study. Therefore, the two different electrodes

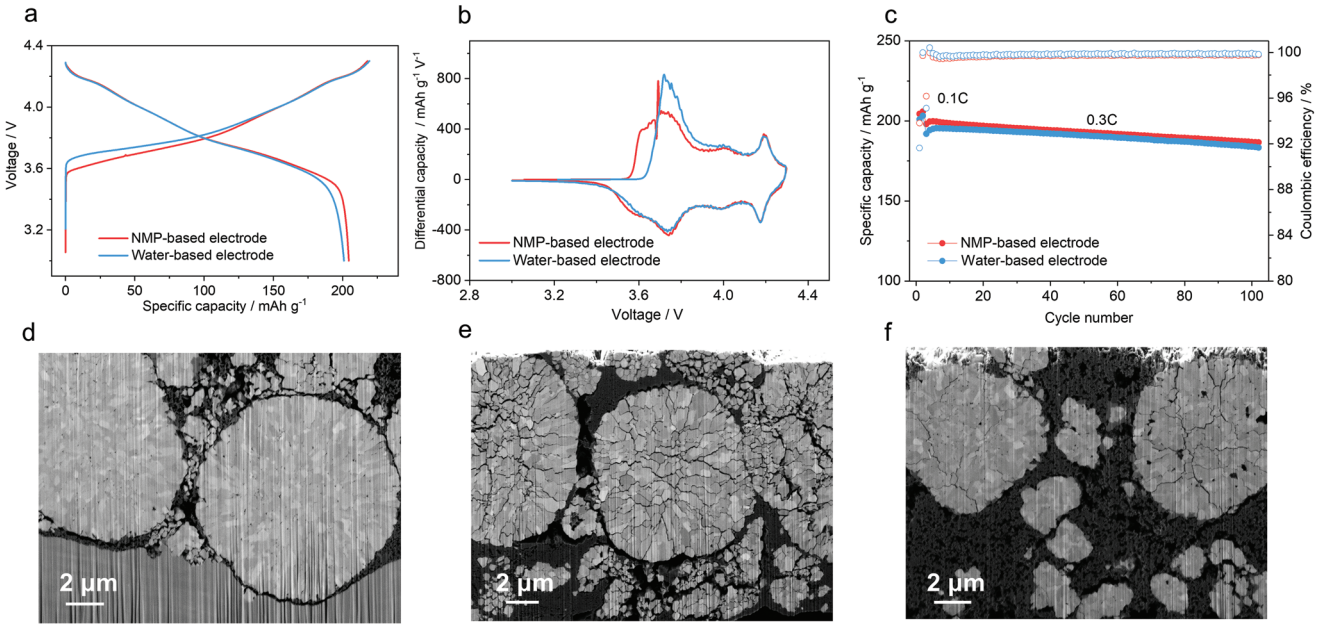

Figure 2. Electrochemical performance of NMP-based and water-based electrodes, made using PVdF and TRD/CMC as binder, respectively, in LP30 electrolyte. a) Charge/discharge profiles and b) differential capacity curves during the first cycle, c) cycling performance at 0.3 C, cross-sectional SEM images of d) an as-made water-based electrode, and e) NMP-based and f) water-based electrodes after 200 cycles at 1 C in LP30. The corresponding capacity performance has been tested on at least three cells with a standard deviation below 5%.

were tested in conventional organic electrolyte (LP30) and their electrochemical performance is shown in **Figure 2**. First, the initial charge/discharge curves recorded at 0.1 C are compared in Figure 2a. At the start of the charge step, a higher steep increase of the voltage up to 3.72 V is observed for the water-based electrode, while 3.56 V is reached for the NMP-based electrode; the origin for this difference is mainly associated with the additional Li_2CO_3 layer on the particle surface generated during electrode processing, the Li_2CO_3 layer hinders the lithium ion transportation.[30] After the initial relatively higher voltage of the water-based electrode, the curve approaches and finally overlaps with that of the NMP-based electrode in the high voltage region, leading to a similar charge capacity. During discharge, the two curves are identical for most of the processes, however, the water-based electrode shows a slightly faster voltage drop toward the end, which is likely due to partial lithium leaching upon water contact during aqueous processing. This leads to a slightly lower discharge capacity of the water-based electrode (201 mAh g^{-1}) compared to the PVdF electrode (204 mAh g^{-1}). Correspondingly, the former achieves a slightly lower Coulombic efficiency (CE) of 91.6% than the latter (93.8%) in the first cycle. The differential capacity plots reveal these slight variations in more detail (Figure 2b). The anodic peak shifts to around 3.7 V in the water-based electrode, consistent with the voltage profile. However, when comparing the curves of the 2nd cycle (Figure S7, Supporting Information), the difference between the two electrodes is nearly negligible, which suggests that Li_2CO_3 has decomposed during the first charge.[31] Nevertheless, this has no negative impact on the cycling stability at 0.3 C (Figure 2c). In general, the two curves show a very similar trend except for a slightly lower capacity for the water-based electrode. This indicates that the aqueous processing of the high nickel content active material did not result in a bulk structural damage beyond its surface composition. The CE values of the water-based electrode are very close to those of the NMP-based electrode (average CE during 100 cycles: 99.8% vs 99.7%). The rate capability of an exemplary water-based electrode is also illustrated in Figure S8 in the Supporting Information, showing high specific discharge capacity of 128 mAh g^{-1} at 5 C and 84 mAh g^{-1} at 10 C. Since thick electrodes are critical to improve the cells energy density through minimizing the inactive component ratio,[32,33] high areal loading water-based electrodes were prepared (≈25 mg cm^{-2}) with thickness of 155 µm (Figure S9, Supporting Information). The preliminary test of such an electrode demonstrates a high discharge capacity (about 5.2 mAh cm^{-2}), showing that the aqueous binder can indeed ensure good mechanical stability and electrochemical performance also for more practical electrode loadings. To obtain more information on morphological changes of the nickel-rich active material during cycling, the cycled electrodes were recovered and characterized by cross-sectional SEM imaging after focused ion-beam (FIB) polishing (Figure 2d–f). In general, the strong structural variations during cycling are expected to lead to the formation of microcracks in the secondary particles. The SEM image of the NMP-based electrode (Figure 2e) reveals that the large primary particles (≈10 µm) have suffered strong damage and plenty of microcracks appear along the grain boundaries. In direct comparison, the situation is slightly improved for the water-based electrode (Figure 2f, more detailed comparison, see Figure S10, Supporting Information), where the microcracks along grain boundaries are not as pronounced, possibly due to the superior surface protection by the phosphate covered layer.

Although the phosphate coating can protect the active material during aqueous processing to achieve practically the same cycling stability as compared to traditional electrode processing,

it cannot avoid the capacity degradation due to the formation of microcracks (Figure 2f). This is not surprising since the inherent problems that cause the serious performance fading have not been fully addressed. First, the lithium salt $LiPF_6$ in LP30 electrolyte easily reacts with trace water and releases reactive hydrogen fluoride (HF), which is prone to attack the cathode surface and leads to structural transformation. It is reasonable to assume that the residual water content might be higher after aqueous electrode processing if no rigorous drying processes are applied.[34] However, from a commercial perspective, such drying substantially increases the cost of electrode manufacturing. Second, the highly reactive Ni^{4+} present at high state of charge is also susceptible to react with the organic electrolyte solvent and aggravate its decomposition. Therefore, the use of a suitable electrolyte, which is not as sensitive to moisture and has a higher stability against Ni^{4+}, would be beneficial for the application of aqueous electrode processing technology. In this regard, we have previously reported on the excellent compatibility with lithium metal and stability of lithium bis(trifluoromethanesulfonyl)imide-based ILEs, which offer an excellent strategy to mitigate the structural transformation of lithium-rich and layered oxide cathodes. The absence of HF or rather reaction pathways to form HF, not only led to the formation of a more robust cathode electrolyte interphase which could significantly mitigate microcrack formation in high nickel content cathodes,[35] but should also make the electrolyte less prone to moisture. Hence, the dual anion ILE ($0.8Pyr_{14}FSI$-0.2LiTFSI) was employed for further investigations with the aqueous processed electrodes. **Figure 3**a compares the cycling performance of water-based electrodes in LP30 and ILE. The results show that the discharge capacity in ILE is initially slightly lower than in LP30 (197 mAh g^{-1} vs 201 mAh g^{-1}). At an increased rate of 0.3 C, this capacity difference is amplified due to the relatively lower ionic conductivity of ILE. However, the cell in ILE shows superior cycling stability with practically no capacity fading during cycling. This becomes even clearer, when directly comparing the voltage profiles of selected cycles (Figure 3b). For the LP30 cell, the discharge curve of the 3rd cycle is still overlapping with that of the 50th cycle, while the curve of the 100th cycle already shows a large deviation from that of the 50th cycle. In contrast, the curves of the 3rd to the 100th cycle in ILE are almost completely overlapping. The differential capacity plots in Figure 3c further corroborate the excellent reversibility of the $Ni^{2+/3+/4+}$ redox couples during cycling. Especially, the high

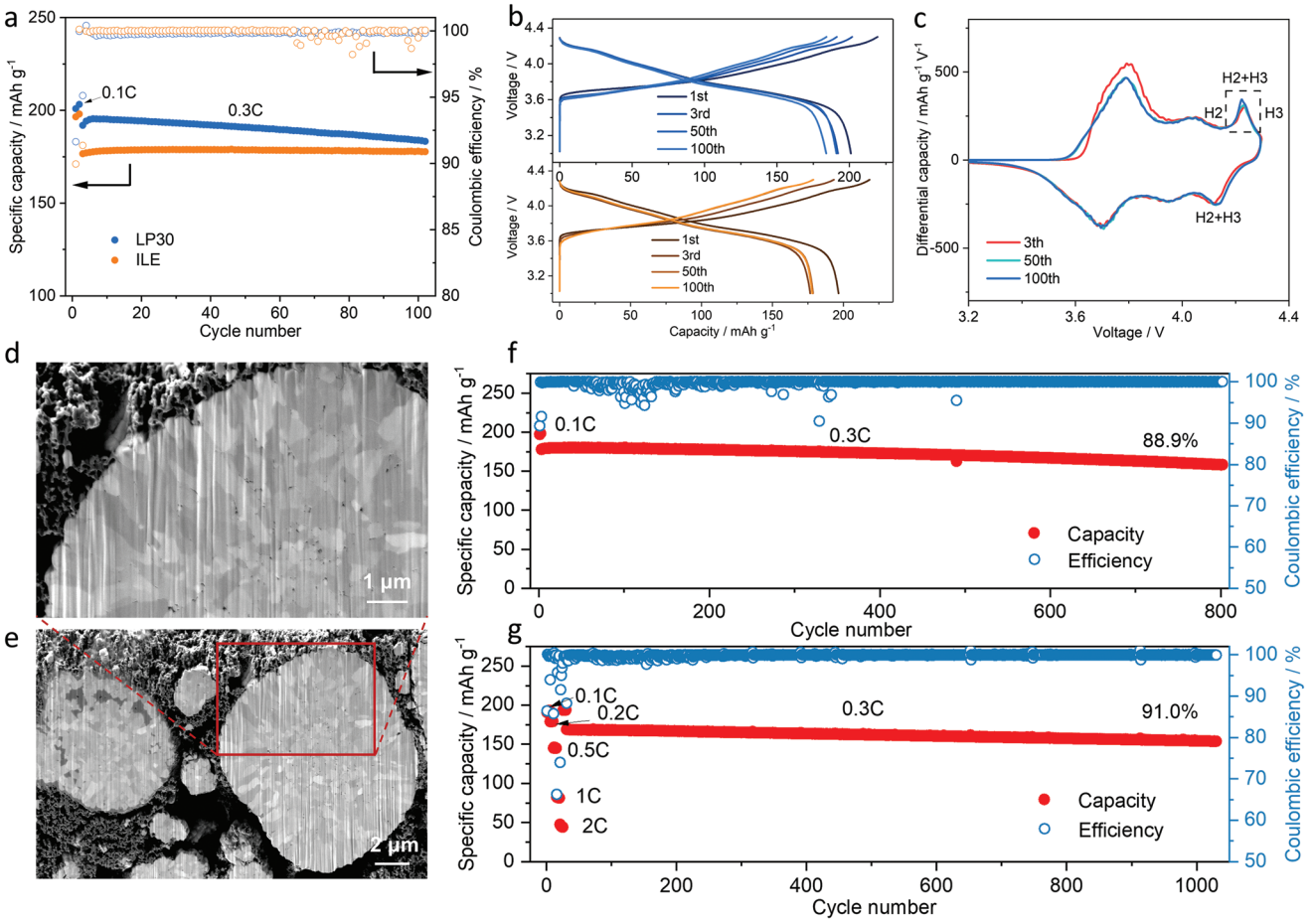

Figure 3. Characterization of water-based NCM811 electrodes in combination with the ILE. a) Cycling performance of water-based electrodes in LP30 and ILE. b) Selected voltage profiles recorded during 100 cycles in LP30 (top) and ILE (bottom). c) Differential-capacity curves for selected cycles in ILE. d,e) Cross-sectional SEM micrographs of cycled water-based electrodes in ILE. Long-term cycling performance of water-based electrodes in ILE at f) 30 °C and g) 20 °C. The corresponding long-term cycling performance has been tested on at least three cells with a standard deviation below 5%.

voltage region representing the phase transformation from hexagonal H2 to hexagonal H3, which is responsible for the strong anisotropic strain and thus, the main reason for microcrack formation, appears to be highly reversible and extremely stable in ILE. The cross-sectional SEM images in Figure 3d,e present the well-maintained secondary particle architecture without any microcracks (see the cross-sectional SEM image in Figure S11, Supporting Information), confirming that the use of this ILE could significantly stabilize the structure of nickel-rich cathodes even using aqueous electrode processing strategies. To further demonstrate the excellent cycling stability of a Li/ILE/NCM811 cell, long-term cycling and rate-capability tests were conducted as shown in Figure 3f,g. The cells maintain an excellent cycling stability and capacity for up to 1000 cycles. After 800 deep dis-/charge cycles at 0.3 C and 30 °C, they show a capacity retention of 88.9%, which corresponds to an irreversible discharge capacity loss of only 0.025 mAh g^{-1} per cycle. The CE stays close to 100%, except for some noise occurring around the 100th cycle probably associated with the formation of soft dendrites. To evaluate the rate capability of the water-based electrodes in ILE, the cells were tested at a lower temperature (20 °C) in a specific current range from 20 to 400 mA g^{-1}, delivering specific discharge capacities of 191 mAh g^{-1} @ 20 mA g^{-1}, 179 mAh g^{-1} @ 40 mA g^{-1}, 145 mAh g^{-1} @ 100 mA g^{-1}, 83 mAh g^{-1} @ 200 mA g^{-1}, and 48 mAh g^{-1} @ 400 mA g^{-1}. The relatively low capacity especially at higher (dis-)charge rates is due to the high viscosity of ILE at 20 °C, but increasing the temperature to only 30 °C already leads to substantial improvement (see Figure S12, Supporting Information). Despite the slightly lower capacities, these measurements reveal an even better cycling stability with a capacity retention of 91.0% after 1000 cycles at 0.3 C.

To elucidate the origin of the superior electrochemical performance in ILE, we investigated the evolution of the lattice parameters during cycling, since the formation of microcracks generally is associated with the variation of lattice parameter at the unit cell level. For this purpose, operando XRD measurements were carried out to trace the structural change of NCM811 particles during the charge process. The cells were charged at a very low current rate (<0.05 C) and the corresponding voltage profiles are presented alongside the evolution of the (003) and (104) reflections in both electrolytes (**Figure 4**a,b). In both cases, the shift of the (003) reflex can be

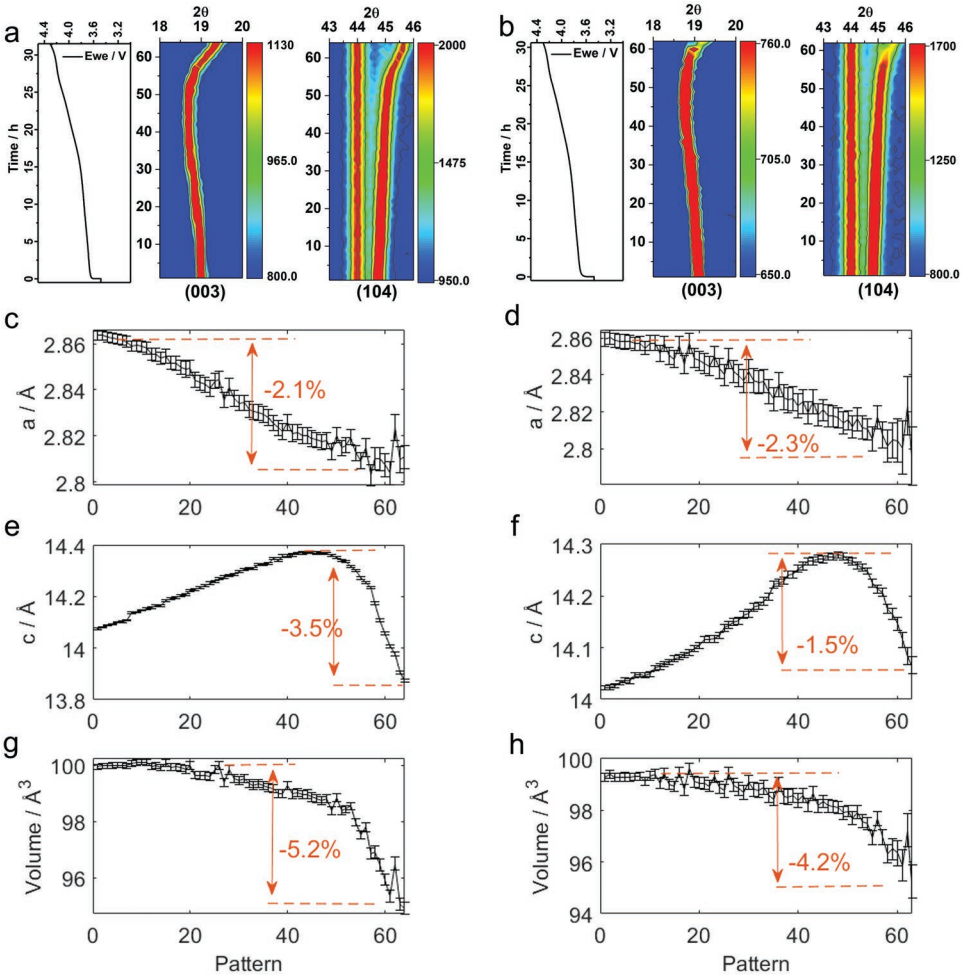

Figure 4. Structural strain evolution of NCM811 during the first charge process in a,c,e,g) LP30 and b,d,f,h) ILE. The lattice parameter change is calculated from sequential Rietveld refinement of the operando XRD measurements following the trend of the shift in (003) and (104) reflections. The corresponding operando measurement was performed on one specific cell.

divided into two regions. The first region is from open circuit voltage to ≈4.1 V, where it shifts to slightly lower angles, which indicates a gradual enlargement of the interlayer or slab distance.[36] In the second region (4.1–4.3 V), a sharp inversion to higher angles is observed, which is ascribed to the phase transformation from hexagonal H2 to H3 phase. In contrast, the (104) reflex follows a continuous shift to higher angles, which increases sharply in the high voltage range. When comparing the peak shift in the second region, it can be easily found that the degree of shift of the (003) and (104) reflections in LP30 is much more pronounced than in ILE, which means that the lattice variation due to the phase transformation is much larger in LP30 than in ILE. By the sequential refinement of the individual in operando recorded XRD patterns, the lattice variation can be quantified, namely, by means of the relative change of the lattice parameters *a*, *c* and unit cell volume *V* as shown in Figure 4c–h. In general, the lattice parameters show a similar, decreasing trend in LP30 and ILE. While the contraction of *a* is very similar (2.1% vs 2.3%), the degree of *c* contraction is significantly different, the value of *c* contraction in LP30 is almost double that in ILE at the highly charged state. This strong contraction along the *c*-axis (3.5%) brings about certain mechanical strain that is intensified by the anisotropy despite a relatively low contraction in the *a*-axis (2.1%). This anisotropic strain contributing to a larger variation of the unit cell volume (ΔV) in LP30 (5.2%) compared to ILE (4.2%) results in the generation of microcracks along the grain boundaries. Furthermore, it is not such a severe issue in the ILE since the contraction extent from *a*-axis and *c*-axis is very close (2.3% vs 1.5%) here. Therefore, microcracks are practically absent in the NCM811 particles even after very long cycling in ILE.

Although the water-processed nickel-rich electrodes show remarkable cycling stability, they still suffer from the high viscosity and conversely low ionic conductivity of the ILE, which limits the electrode mass loadings far from practical application. However, the introduction of small organic molecules such as additives can reduce the degree of coordination of the lithium ion by the anion of the ionic liquid, i.e., facilitating the ion mobility and improving ionic conductivity.[37,38] We therefore modified our ILE via the addition of small amounts of EC and VC, which are common solvents or additives for organic electrolytes.[39,40] First, the ionic conductivity of pure ILE and that of a mixture with either 5% EC or 5% VC as additive in the ILE were measured at different temperatures ranging from −30 to 80 °C (**Figure 5**a). The results show that the conductivity has slightly improved with 5% EC additive and increased even more with the addition of 5% VC additive. Furthermore, this increase is more pronounced at lower temperatures. For an operation temperature of 30 °C, the value increases from 3.11 mS cm^{-1} in pure ILE to 4.05 mS cm^{-1} with 5% VC additive, which is expected to enhance the lithium diffusion in thicker electrodes. With regard to the compatibility toward lithium metal, the pure ILE already proved to have an excellent stability upon prolonged stripping/plating cycling.[20] This is also corroborated by our tests with a symmetric Li cell (Figure 5b). Furthermore, this measurement shows that the overvoltage in ILE with 5% EC additive is increasing continually, indicating the formation of an unstable solid electrolyte interphase (SEI) layer on the

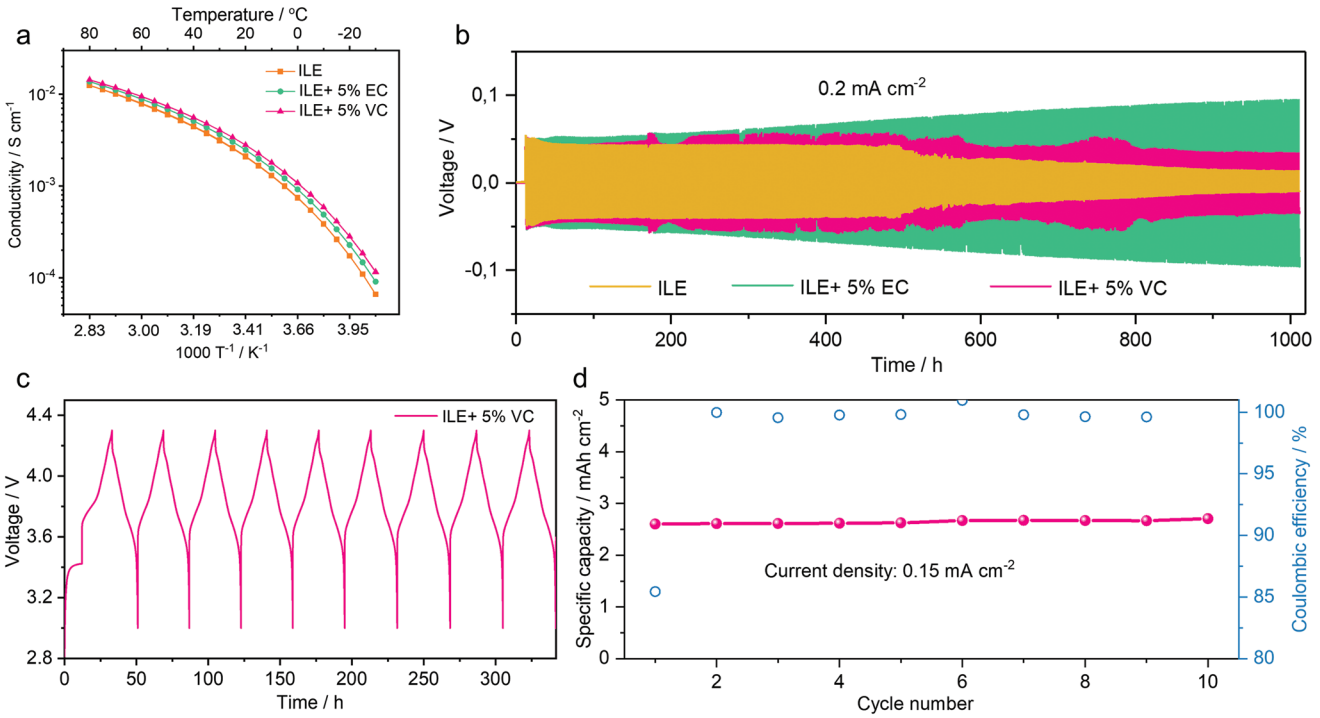

Figure 5. Investigation of the effect of different additives for ILE. a) Ionic conductivity and b) Li-metal stripping-plating behavior in the pure ILE, and with 5% EC or 5% VC additive. c) Voltage versus time profiles and d) charge/discharge cycling performance in a Li|ILE+5%VC|NCM811 cell with a thin lithium metal (25 µm) anode at a current of 0.15 mA cm^{-2}. The corresponding stripping-plating and capacity performance has been tested on two cells with a standard deviation below 5%.

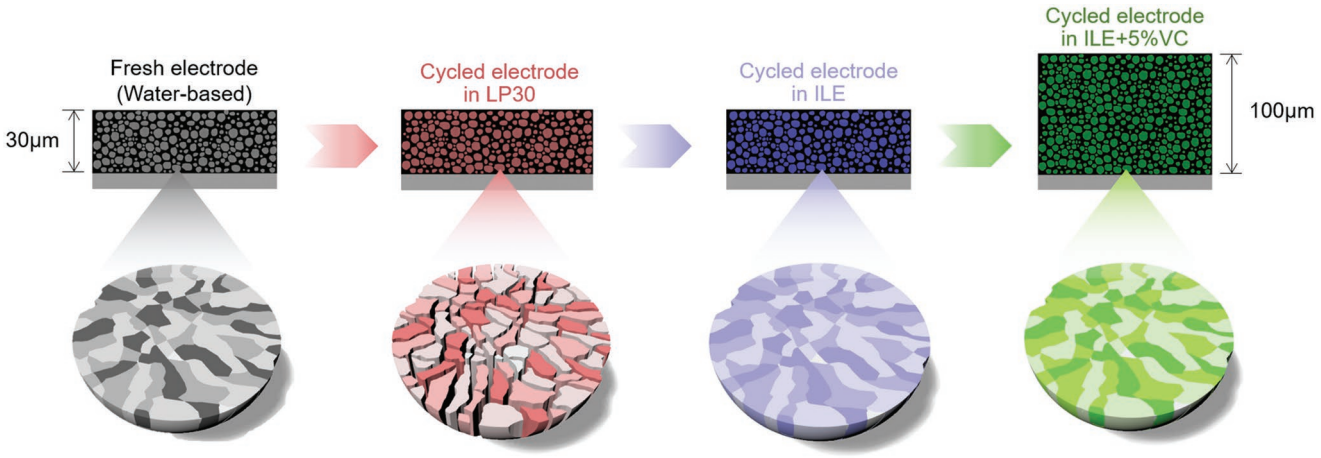

Figure 6. Schematic of the active material particle transformation occurring in high-mass loading NCM811 positive electrodes prepared with water-soluble binders as a function of the electrolyte employed.

lithium metal interface due to the adventitious EC additive. In contrast, the overvoltage in ILE with 5% VC additive does not increase, demonstrating that the modified electrolyte still maintains a stable interface with lithium metal. Finally, the 5% VC containing ILE was employed for the cycling of an aqueous processed high loading Ni-rich electrode. The cells were built combining thick positive electrodes (≈15 mg cm^{-2}) with thin (25 µm) lithium metal anode. The voltage evolution upon cycling (Figure 5c) shows that the cells exhibit a well-reversible intercalation and deintercalation. The discharge capacity is stable above 2.5 mAh cm^{-2} at a current density of 0.15 mA cm^{-2} and the cells possess a high CE (>99.5%) (Figure 5d). All this demonstrates that the VC additive is not only beneficial to lithium diffusion but also helps to build a stable SEI layer in the high loading electrodes.

Summarizing, the combination of the environmentally friendly aqueous electrode processing of nickel-rich cathodes with the poorly volatile and nonflammable ionic liquid-based electrolyte enables cells with high areal capacities (>2.5 mAh cm^{-2}) and excellent cycling stability (>91% capacity retention after 1000 cycles) due to the suppression of the morphological and structural transformations of the active electrode material as shown in **Figure 6**.

3. Conclusion

We were able to demonstrate a high-energy lithium metal battery with high cycling stability using a nickel-rich cathode obtained through an aqueous electrode manufacturing process. The water-processed electrodes (including thick electrodes >20 mg cm^{-2}) are made with a mixture of TRD202A and CMC as binder and phosphoric acid as slurry additive to establish a phosphate coating layer on the surface of the electrode particles. The electrodes show excellent electrochemical performance when directly compared to traditional electrode processing with hazardous NMP solvent and PVdF binder. To address the remaining capacity degradation observed for both binder systems, an ionic liquid-based electrolyte is employed together with the water-processed electrodes. This leads to a dramatic improvement in cycling stability that totally offsets the effect of electrode processing, i.e., the lithium metal cells achieve more than 91% capacity retention and a high CE over more than 1000 cycles at 20 °C. Nevertheless, the ILE is limited by its relatively high viscosity and thus low ionic conductivity, which hinders its commercialization. To overcome these drawbacks, the ILE is modified by addition of 5% VC, delivering a high capacity of more than 2.5 mAh cm^{-2} in high mass loading electrodes (≈15 mg cm^{-2}). In conclusion, our work outlines a pathway for the practical implementation of both NMP-free electrode processing and safe nonflammable ILEs in lithium-metal batteries with improved sustainability.

4. Experimental Section

Sample Preparation: The water-based electrodes were prepared by mixing the active material (NCM811), conductive carbon (Super C45, IMERYS), TRD202A (JSR), and CMC (Walocel CRT 2000 PPA 12) binders in a weight ratio of 91:5:3:1. In addition, phosphoric acid (1 wt% with respect to all solids in the slurry) was added to protect the positive electrode (material) and inhibit the corrosion of the Al current collector. The slurry (solid content ≈60%) was made using deionized water (Millipore ion-exchange resin deionizer) as dispersant/solvent. After homogenization, the slurry was cast onto aluminum foil (15 µm). The coated slurry was dried in an oven (80 °C) for ≈10 min and then in the dry room overnight. After that the electrodes were punched into disks of 12 mm diameter and finally dried again under vacuum at 110 °C for 12 h. For reference, NMP-based electrodes were prepared by mixing NCM811, Super C65 (IMERYS), and PVdF (Solef 6020, Solvay) in the weight ratio of 92:4:4, using NMP (anhydrous, >99.5%; Sigma-Aldrich) as dispersant/solvent. After drying in dry air overnight (dew point <–60 °C, i.e., inside dry room), the electrodes were punched into disks of the same diameter (12 mm) and vacuum dried at 120 °C for 12 h. Finally, all electrodes were pressed at 5 ton cm^{-2} (except when specified). The average areal mass loading was around 3.2 ± 0.2 mg cm^{-2}, except for the preliminary tests on high mass loading samples (≈25 mg cm^{-2} in LP30 electrolyte, ≈15 mg cm^{-2} in ILE (0.8Pyr_{14}FSI-0.2LiTFSI) with VC additive). The lithium-coated copper foil (25 µm Li) was punched into disks of 12 mm diameter. The ILE was prepared by dissolving LiTFSI (battery grade, 99.5 wt%, 3 м) in Pyr_{14}FSI in a molar ratio of 2:8. The neat ionic liquid was predried at 80 °C in a tubular vacuum oven (Büchi), remaining volatile compounds were then removed at RT and 80 °C by a turbo molecular pump ($P < 10^{-7}$ mbar). In addition, either 5 wt% EC or

5 wt% VC was added to the ILE as additives. The commercially available electrolyte (LP30, Selectilyte, BASF) consisting of 1 M $LiPF_6$ in a mixture of EC and DMC (1:1 by volume) was chosen for comparison. Its water content was below 15 ppm.

Electrochemical Measurements: The electrochemical performance of lithium metal cells employing LP30 and ILE upon galvanostatic cycling was evaluated in two-electrode pouch cells (the pouch size is 10 mm × 10 mm), which were assembled in the dry room using Whatman glass fiber sheets (GF/A) as separator and lithium metal disks (thickness 500 µm) as negative electrode, with ≈120 µL corresponding electrolyte. Galvanostatic cycling was performed using a Maccor battery tester 4300. NCM811 electrodes were cycled between 3.0 and 4.3 V at 0.1 C during the first two (formation) cycles, and then at 0.3 C. The (dis-)charge rate of 1 C corresponds to a specific current of 200 mA g^{-1}. Except when specifically mentioned, all electrochemical measurements were performed in climatic chambers at 30 ± 2 °C.

Statistical Analysis: Cell data were statistically analyzed using the MimsClient software. The voltage versus time curves were primary test data obtained from Maccor battery tester 4300, the corresponding capacity curves were secondary test data calculated and transformed from the primary test data. The presented capacity data of the cells in each graph corresponded to one specific cell. However, each capacity data was evaluated on at least two additional cells with a standard deviation below 5%.

Materials Characterization: The morphology and structure of the NCM811 powder and electrodes were investigated by SEM (ZEISS Crossbeam XB340 equipped with an EDX detector). To investigate the internal structure of the electrode and active material particles, cross-sections were prepared using a Capella FIB (gallium ion source) system with milling and polishing currents of 30 and 3 nA, respectively, at an acceleration voltage of 30 kV, respectively. All samples recovered from cycled cells were transferred to the microscope under argon atmosphere using an air-tight transfer box (Sample Transfer Shuttle, SEMILAB). Micrographs were acquired from the top and in cross-sectional configuration (under a tilt-angle of 54°) after FIB preparation using smart SEM software for tilt correction to compensate for the image distortion due to the tilt of 54° to the optical axis. XPS was carried out on a Specs XPS system with a Phoibos 150 energy analyzer using monochromatic Al K_α radiation (1486.6 eV), a take-off angle of 45°, and pass energies of 30 and 90 eV at the analyzer for detail and survey spectra, respectively. For sample preparation, the cycled electrodes were thoroughly washed with DMC, dried, and transferred under inert gas to the XPS system. The samples were either investigated directly or after Ar^+ ion sputtering for 30 min (≈0.1 nm min^{-1} sputter rate, 0.1 µA, 5 kV). Casa XPS was used for data analysis, using Shirley-type backgrounds and Gaussian-Lorentzian peak shapes. All XPS spectra were calibrated to the C (1s) peak of conductive C additive/adventitious C (C—C/C—H species) at 284.8 eV.

The conductivity of the ILE was measured by a conductometer equipped with a frequency analyzer and a thermostatic bath (MMates Italia). The electrolyte was sealed in glass conductivity cells (assembled in the glove box) equipped with two platinized platinum electrodes. The cell constant was determined using a 0.01 M KCl standard solution. The measurements were performed in the temperature range from –30 to 80 °C and recorded every 5 °C. The equilibration time at each temperature was set to 1 h.

Operando XRD experiments were performed using a test cell (ECC-Opto-Std, EL cell) with a Mylar film window on a Bruker D8 Advance diffractometer (Cu K_α radiation (λ = 0.15406 nm) in the 2θ range between 16° ≤ 2θ ≤ 72° with a step size of 0.046° and a 1.48 s per point acquisition time. During slow charge (7 mA g^{-1} for both electrolytes) to 4.3 V, XRD patterns were continuously recorded every 30 min. For these tests, the positive electrodes were prepared by casting the electrode slurry (the same ratio of components as before) on aluminum mesh (diameter: 16 mm). The electrodes were stored in the dry room overnight, then further dried under vacuum at 120 °C for 12 h.

XRD patterns were recorded on a Bruker D8 diffractometer equipped with a Cu Kα source (λ = 0.15406 nm) in the 10° < 2θ < 140° range with a step size of 0.010° and a 1.43 s per point acquisition time for the powder sample . Rietveld refinement of the XRD patterns of the powder samples was conducted in the 14° < 2θ < 140° range using GSAS-II software.[41] The structural model reported by Zheng et al.[42] was modified according to the actual stoichiometry of the NCM811 material, i.e., by considering a fixed elemental composition ratio of Ni:Mn:Co = 80:10:10. The background was fitted with a Chebyshev polynomial function with eight coefficients. The instrumental parameters were obtained from a LaB_6 standard; accordingly, the instrumental broadening parameters, i.e., *U*, *V*, *W*, *X*, and *Y*, were kept fixed to 4.397×10^{-4}, -5.720×10^{-4}, 2.577×10^{-4} deg^2, 1.855×10^{-2} deg, and 2×10^{-5} deg, respectively. The peak shape was refined with anisotropic microstrain broadening model and by optimizing the respective parameter, calculated as a unitless fraction of $\Delta d/d \times 10^6$ (being *d* the interplanar distance) and due only to the sample. The scale, background, sample displacement, unit cell parameters, peak shape, and atomic parameters were refined in this order. Sequential Rietveld refinement of the in situ datasets was performed in the 18° < 2θ < 72° range by considering as the structural model the one obtained for the NCM811 powder and by fixing the atomic parameters. The instrumental parameters were kept fixed as for the powder, while the peak shape was refined by optimizing the isotropic microstrain model parameter. The scale, background, unit cell parameters, and peak shape were refined in this order.

Supporting Information

Supporting Information is available from the Wiley Online Library or from the author.

Acknowledgements

F.W. gratefully acknowledges financial support from the Chinese Scholarship Council (CSC). The authors acknowledge financial support from the Helmholtz Association and the German Federal Ministry of Education and Research (BMBF) within the LILLINT (03XP0225D) project. J.-K.K. acknowledges the support from the National Research Foundation of Korea (NRF) grant funded by the Korea government (MSIT) (NRF-2020R1A2C2009057, NRF- 2021R1A4A200168711). The authors are very grateful to Dr. Xinpei Gao for supplying the ionic liquid.

Open access funding enabled and organized by Projekt DEAL.

Conflict of Interest

The authors declare no conflict of interest.

Author Contributions

F.W. prepared the electrodes, performed the (in situ) XRD characterization and electrochemical measurements, and drafted the manuscript. M.K. performed the cross-sectional SEM measurements and revised the manuscript. T.D. performed and analyzed the XPS measurements and revised the manuscript. A.M. performed the refinement of the in situ XRD measurements. S.F. contributed experimental discussion and revised the manuscript. J.-K.K. supplied the NCM811 materials. H.-W.K. performed the schematic drawing. G.-T.K. conceptualized the activities, supervised the experimental work, and revised the manuscript. S.P. conceptualized and coordinated the activities, provided funding for the work, and revised the manuscript.

Data Availability Statement

The data that support the findings of this study are available on request from the corresponding author. The data are not publicly available due to privacy or ethical restrictions.

Keywords

aqueous binders, ionic liquid electrolytes, lithium batteries, lithium metal, Ni-rich cathodes

Received: June 22, 2022
Revised: August 16, 2022
Published online: September 18, 2022

[1] J. Liu, H. Yuan, X. Tao, Y. Liang, S. J. Yang, J. Q. Huang, T. Q. Yuan, M. M. Titirici, Q. Zhang, *EcoMat* **2020**, *2*, e12019.
[2] N. Loeffler, G.-T. Kim, F. Mueller, T. Diemant, J.-K. Kim, R. J. Behm, S. Passerini, *ChemSusChem* **2016**, *9*, 1112.
[3] D. Bresser, D. Buchholz, A. Moretti, A. Varzi, S. Passerini, *Energy Environ. Sci.* **2018**, *11*, 3096.
[4] T. Tanabe, T. Gunji, Y. Honma, K. Miyamoto, T. Tsuda, Y. Mochizuki, S. Kaneko, S. Ugawa, H. Lee, T. Ohsaka, F. Matsumoto, *Electrochim. Acta* **2017**, *224*, 429.
[5] P. Zuo, W. Yang, X. Cheng, G. Yin, *Ionics* **2010**, *17*, 87.
[6] Q. Wu, S. Ha, J. Prakash, D. W. Dees, W. Lu, *Electrochim. Acta* **2013**, *114*, 1.
[7] M. Hofmann, M. Kapuschinski, U. Guntow, G. A. Giffin, *J. Electrochem. Soc.* **2020**, *167*, 140512.
[8] W. Li, E. M. Erickson, A. Manthiram, *Nat. Energy* **2020**, *5*, 26.
[9] A. R. Schuer, M. Kuenzel, S. Yang, M. Kosfeld, F. Mueller, S. Passerini, D. Bresser, *J. Power Sources* **2022**, *525*, 231111.
[10] W. Liu, P. Oh, X. Liu, M. J. Lee, W. Cho, S. Chae, Y. Kim, J. Cho, *Angew. Chem.* **2015**, *54*, 4440.
[11] N. Loeffler, J. von Zamory, N. Laszczynski, I. Doberdo, G.-T. Kim, S. Passerini, *J. Power Sources* **2014**, *248*, 915.
[12] Z. Chen, G.-T. Kim, D. Chao, N. Loeffler, M. Copley, J. Lin, Z. Shen, S. Passerini, *J. Power Sources* **2017**, *372*, 180.
[13] Z. Wang, N. Dupré, A.-C. Gaillot, B. Lestriez, J.-F. Martin, L. Daniel, S. Patoux, D. Guyomard, *Electrochim. Acta* **2012**, *62*, 77.
[14] T. Dong, H. Zhang, Y. Ma, J. Zhang, X. Du, C. Lu, X. Shangguan, J. Li, M. Zhang, J. Yang, X. Zhou, G. Cui, *J. Mater. Chem. A* **2019**, *7*, 24594.
[15] M. Kuenzel, R. Porhiel, D. Bresser, J. Asenbauer, P. Axmann, M. Wohlfahrt-Mehrens, S. Passerini, *Batteries Supercaps* **2019**, *3*, 155.
[16] M. Kuenzel, D. Bresser, G.-T. Kim, P. Axmann, M. Wohlfahrt-Mehrens, S. Passerini, *ACS Appl. Energy Mater.* **2019**, *3*, 218.
[17] J.-H. Kuo, C.-C. Li, *J. Electrochem. Soc.* **2020**, *167*, 100504.
[18] M. Wood, J. Li, R. E. Ruther, Z. Du, E. C. Self, H. M. Meyer, C. Daniel, I. Belharouak, D. L. Wood, *Energy Storage Mater.* **2020**, *24*, 188.
[19] M. Stich, M. Göttlinger, M. Kurniawan, U. Schmidt, A. Bund, *J. Phys. Chem. C* **2018**, *122*, 8836.
[20] F. Wu, G. T. Kim, T. Diemant, M. Kuenzel, A. R. Schür, X. Gao, B. Qin, D. Alwast, Z. Jusys, R. J. Behm, D. Geiger, U. Kaiser, S. Passerini, *Adv. Energy Mater.* **2020**, *10*, 2001830.
[21] J. Li, C. Daniel, S. J. An, D. Wood, *MRS Adv.* **2016**, *1*, 1029.
[22] D. L. Wood, J. D. Quass, J. Li, S. Ahmed, D. Ventola, C. Daniel, *Drying Technol.* **2017**, *36*, 234.
[23] F. Wu, A. R. Schür, G.-T. Kim, X. Dong, M. Kuenzel, T. Diemant, G. D'Orsi, E. Simonetti, M. De Francesco, M. Bellusci, G. B. Appetecchi, S. Passerini, *Energy Storage Mater.* **2021**, *42*, 826.
[24] G. A. Elia, U. Ulissi, S. Jeong, S. Passerini, J. Hassoun, *Energy Environ. Sci.* **2016**, *9*, 3210.
[25] W. Porcher, B. Lestriez, S. Jouanneau, D. Guyomard, *J. Electrochem. Soc.* **2008**, *156*, A133.
[26] P. Zou, Z. Lin, M. Fan, F. Wang, Y. Liu, X. Xiong, *Appl. Surf. Sci.* **2020**, *504*, 144506.
[27] M. Kuenzel, D. Bresser, T. Diemant, D. V. Carvalho, G. T. Kim, R. J. Behm, S. Passerini, *ChemSusChem* **2018**, *11*, 562.
[28] S.-W. Lee, M.-S. Kim, J. H. Jeong, D.-H. Kim, K. Y. Chung, K. C. Roh, K.-B. Kim, *J. Power Sources* **2017**, *360*, 206.
[29] W. Zhang, L. Liang, F. Zhao, Y. Liu, L. Hou, C. Yuan, *Electrochim. Acta* **2020**, *340*, 135871.
[30] H. Liu, A. J. Naylor, A. S. Menon, W. R. Brant, K. Edström, R. Younesi, *Adv. Mater. Interfaces* **2020**, *7*, 2000277.
[31] N. Mahne, S. E. Renfrew, B. D. McCloskey, S. A. Freunberger, *Angew. Chem., Int. Ed.* **2018**, *57*, 5529.
[32] Y. Kuang, C. Chen, D. Kirsch, L. Hu, *Adv. Energy Mater.* **2019**, *9*, 1901457.
[33] W. Pfleging, *Int. J. Extreme Manuf.* **2021**, *3*, 012002.
[34] M. Kosfeld, B. Westphal, A. Kwade, *J. Energy Storage* **2022**, *51*, 104398.
[35] F. Wu, S. Fang, M. Kuenzel, A. Mullaliu, J.-K. Kim, X. Gao, T. Diemant, G.-T. Kim, S. Passerini, *Joule* **2021**, *5*, 2177.
[36] F. Wu, G. T. Kim, M. Kuenzel, H. Zhang, J. Asenbauer, D. Geiger, U. Kaiser, S. Passerini, *Adv. Energy Mater.* **2019**, *9*, 1902445.
[37] Z. Li, O. Borodin, G. D. Smith, D. Bedrov, *J. Phys. Chem. B* **2015**, *119*, 3085.
[38] A. Deshpande, L. Kariyawasam, P. Dutta, S. Banerjee, *J. Phys. Chem. C* **2013**, *117*, 25343.
[39] W. Zhao, Y. Ji, Z. Zhang, M. Lin, Z. Wu, X. Zheng, Q. Li, Y. Yang, *Curr. Opin. Electrochem.* **2017**, *6*, 84.
[40] S. S. Zhang, *J. Power Sources* **2006**, *162*, 1379.
[41] B. H. Toby, R. B. Von Dreele, *J. Appl. Crystallogr.* **2013**, *46*, 544.
[42] X. Zheng, X. Li, B. Zhang, Z. Wang, H. Guo, Z. Huang, G. Yan, D. Wang, Y. Xu, *Ceram. Int.* **2016**, *42*, 644.